www.acsnano.org

# Targeted Discovery of Low-Coordinated Crystal Structures via Tunable Particle Interactions

Hillary Pan and Julia Dshemuchadse\*



Downloaded via CORNELL UNIV on April 18, 2023 at 20:31:24 (UTC). See https://pubs.acs.org/sharingguidelines for options on how to legitimately share published articles.

Cite This: https://doi.org/10.1021/acsnano.2c09131



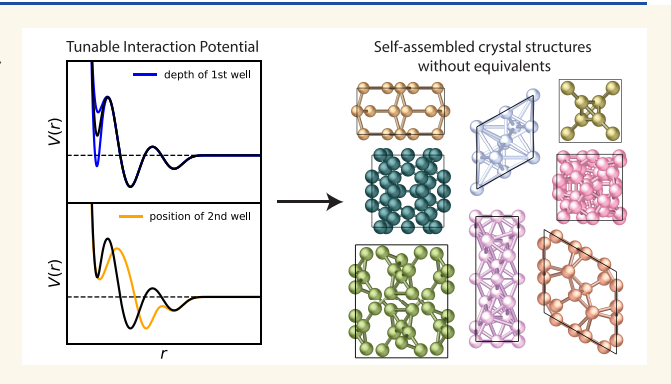
**ACCESS** 

III Metrics & More

Article Recommendations

s Supporting Information

ABSTRACT: Particles interacting via isotropic, multiwell pair potentials have been shown to self-assemble into a range of crystal structures, yet how the characteristics of the underlying interaction potential give rise to the resultant structure remains largely unknown. We have thus developed a functional form for the interaction potential in which all features can be tuned independently. We perform continuous parameter space searches by systematically changing pairs of parameters, controlling the various features of the interaction potential. By enforcing a repulsive first well (controlling particle interactions of the first neighbor shell), we stimulate the formation of low-coordinated assemblies. We report the self-assembly of 20 previously unknown crystal structure types, 14 of which have low



coordination numbers. Despite limiting the search to a small region of the vast parameter space of possible particle interactions, a wealth of complexity and symmetry is apparent within these crystal structures, which include clathrates with empty cages and low-symmetry structures. Our findings suggest that an unknown number of previously undiscovered crystal structure configurations are possible through self-assembly, which can serve as interesting design targets for soft condensed matter synthesis.

KEYWORDS: molecular dynamics, self-assembly, crystal structure, interaction potential, forward design

#### **INTRODUCTION**

The spontaneous self-assembly of molecular building blocks into ordered structures on the mesoscale has increasingly been used to engineer metamaterials with advanced properties. Numerous soft matter building blocks-e.g., surfactants, dendrimers, 2,3 block copolymers, 4,5 and metallic nanoparticles -have been shown to self-assemble into crystal structures on the mesoscale (frequently called "superlattices") that are isostructural to atomic systems, from simple sphere packings to complex aperiodic structures. Unlike atomic-scale ordering, which is limited by chemical makeup and bonding rules, structures that form at larger length scales are not bound by the same constraints, and particles are free to explore a much larger space of possible configurations.7 It is therefore possible to observe not only soft materials that order into familiar patterns<sup>4,8,9</sup> but also structures without atomic equivalents. 10,11

To design self-assembled crystals, it is important to know which structures are feasible as well as the interparticle interactions that will form that structure. For instance, it is well-known that the Lennard-Jones interaction potential, consisting of a steep repulsive interaction followed by a single attractive well, will reliably form high-coordinated, spherepacking structures such as the face-centered cubic close packing (ccp). 12,13 Interaction potentials encoded with longer-range interactions beyond the first neighbor shell, however, are much less predictable and have been shown to produce a diverse range of structures with varying complexity and coordination environments, including a number of previously unknown crystal structures with intermediate coordination numbers 14 (rare in atomic systems) and even a one-component icosahedral quasicrystal. 15

Of particular interest is the self-assembly of particles into open, low-coordinated crystal structures, notably within the

Received: September 13, 2022 Accepted: April 5, 2023



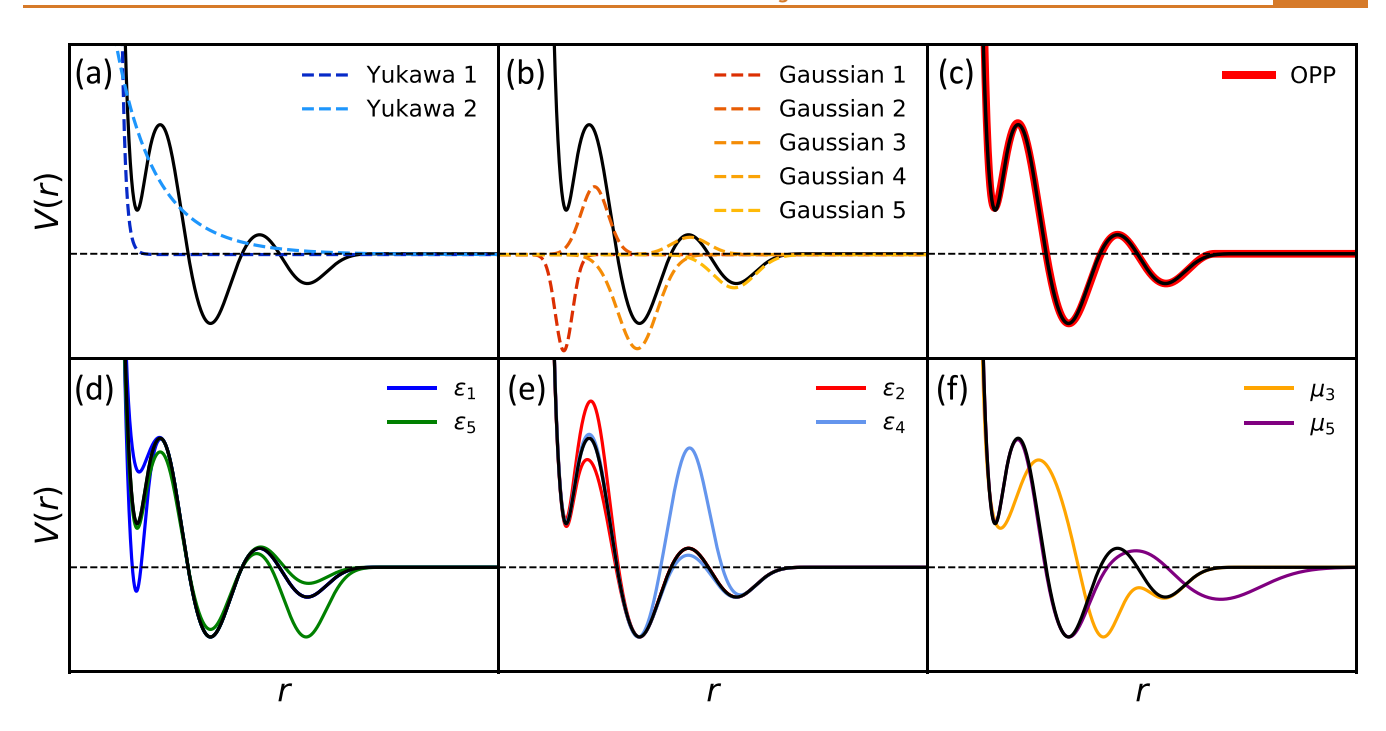


Figure 1. Construction of the Y2G5P using a linear combination of (a) two Yukawa functions and (b) five alternating attractive and repulsive Gaussians. (c) Agreement between the OPP and Y2G5P functions (red and black lines, respectively) leads to the assembly of the same resulting cP54-K<sub>4</sub>Si<sub>23</sub> structure type in the simulation. The features of the Y2G5P are tunable: the minimum and maximum variations in parameters for the depths of the first and third well ( $\epsilon_1$  and  $\epsilon_5$ ), between hump heights ( $\epsilon_2$  and  $\epsilon_4$ ), and positions of the first and third well ( $\mu_3$  and  $\mu_5$ ) are shown in (d), (e), and (f), respectively.

fields of catalysis 16,17 in which porous framework structures such as clathrates, zeolites, and metal-organic frameworks can host guest species, as well as photonics, <sup>18</sup> where self-assembled structures are of technological interest as photonic crystals. The tetrahedrally coordinated diamond structure, for instance, has gained wide attention as an interesting candidate for selfassembly after it was theoretically determined to possess a large omnidirectional photonic bandgap, 19 and it was recently experimentally realized using tetrahedral clusters with sticky patches. In simulation, it was previously believed that such low-coordinated structures would be difficult to model due to their anisotropic bonding environments and thus require complex, multibody, and angle dependent interactions. 20-22 Subsequent studies, however, have proven that known lowcoordinated structures such as simple cubic, 23 diamond, and wurtzite<sup>24</sup> can in fact be simulated using relatively simple, multiwell isotropic pair potentials. More recently, similar pair potentials were used to assemble much more complex, known low-coordinated structures, including several clathrates. <sup>15</sup> Due to the high variability of possible particle interactions on the mesoscale, a remaining question is whether, and to what extent, we can observe low-coordinated structures that have not been observed before and could be of potential technological interest. An exciting possibility is that such structures may be interesting candidates for photonic crystals, since recent literature suggests that the parameter space of spherical particle assemblies that can serve as viable photonic crystals is much larger than previously imagined.<sup>25</sup>

Previously, Dshemuchadse et al. performed comprehensive searches of the two-dimensional parameter spaces of two interaction potentials: the oscillating pair potential (OPP) and the Lennard-Jones—Gauss potential (LJGP). The self-assembled crystal structures comprised 16 known structure

types and 15 that have not been observed before, spanning a diverse range of coordination environments (with average coordination numbers of  $\langle CN \rangle = 4-14$ ). The majority of the previously unknown structures had intermediate coordination numbers ranging from 7 to 11 nearest neighbors, and were mostly present in the LJGP phase diagram, whereas the majority of the low-coordinated structures were only present in the OPP phase diagram. A distinguishing feature between the OPP and LJGP is that the OPP can exhibit a repulsive first well, which we believe to stimulate the formation of lowcoordinated structures, while the LJGP is characterized by its flexible shape due to its functional form. In this work, we build on these findings by creating an interaction potential that possesses the repulsive first well of the OPP while still preserving the tunability of the features, as was the case for the LJGP. We use this interaction potential design to conduct a targeted search for previously unknown low-coordinated assemblies within the vast parameter space spanned by particles interacting via isotropic pair potentials. Within a few thousand simulations, we observe a diverse pool of selfassembled crystal structures, including several low-coordinated structures without atomic equivalents. We report the selfassembly of 20 crystal structure types as well as a quasicrystal, none of which had been observed previously. Additionally, our interaction potential design is both flexible and intuitive, and thus serves as an important step toward connecting the shape of the interaction potential to the resulting structure.

#### **MODEL**

In developing a functional form for interaction potentials, we preserve the simplicity of the pair potential shape while at the same time adding flexibility to tune all of its features independently and in an intuitive manner. As demonstrated

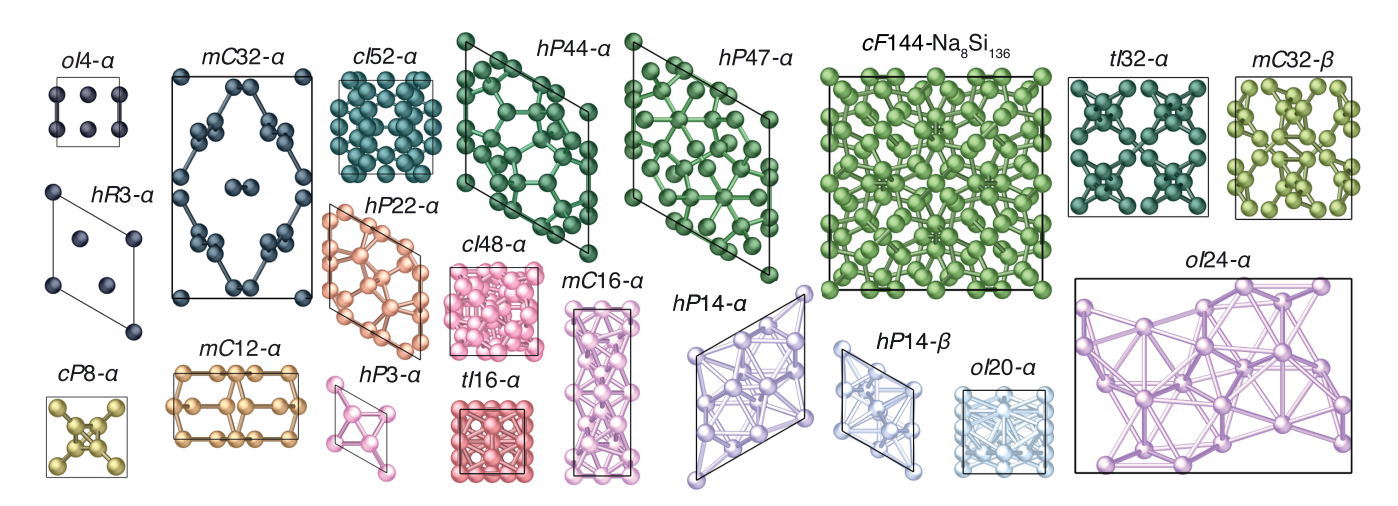


Figure 2. Twenty previously unknown crystal structures found using Y2G5Ps. Structures are labeled using Pearson symbols, which are composed of the Bravais lattice, the number of particles contained in a unit cell, typically followed by the prototypical compound exhibiting such an arrangement of atoms. Here, we use  $\alpha$  and  $\beta$  to indicate that these structures have no known atomic equivalents.

previously by Dshemuchadse et al., introducing multiple competing length scales via two attractive wells is necessary to assemble a variety of crystal structures beyond dense sphere packings (which only require a single attractive well). The assembly of low-coordinated structures is found to emerge when a repulsive first well is enforced, and the lowest-coordinated structures were only possible with a repulsive hump between the first (repulsive) and second (attractive) well. To enable the search for low-coordinated structures, we therefore construct an interaction potential functional form in which the shape of the interaction potential consists of a repulsive first well and two attractive wells, with each of these wells separated by repulsive humps. Our chosen design consists of a linear combination of two Yukawa potentials and five alternating positive and negative Gaussians (Y2GSP):

$$V(r) = \sum_{i=1}^{2} g_{i}^{2} \frac{\exp[-\alpha_{i} m_{i} (r - \mu_{i})]}{r - \mu_{i}} + \sum_{j=1}^{5} (-1)^{j} \epsilon_{j} \exp\left[\frac{(r - \mu_{j})^{2}}{-2\sigma_{j}^{2}}\right]$$

The first term in the equation is a summation of two Yukawa potentials. The Yukawa potential  $V(r) = -g^2 \exp[-\alpha mr]/r$  was originally designed to be used in particle physics to model interactions between protons and neutrons, with m representing particle mass and g and  $\alpha$  as scaling factors. There, we use its mathematical function to control the steepness of the Y2G5P at a lower interparticle distance r, where the function approaches infinity, while adding a  $\mu$  term to control the position of the potentials relative to r. All parameter values of the Yukawa potentials are fixed. We use two Yukawa potentials in order to enforce a positive (i.e., net repulsive) first well: one Yukawa potential serves to create sufficient repulsion at low r, while the other less steep one serves as the "background" on which the first Gaussian sits (see Figure 1a).

The five Gaussians are combined to form a three-well potential with repulsive humps between them, with well depths/hump heights  $\epsilon$ , widths  $\sigma$ , and positions  $\mu$  (see Figure 1b). The second well (i.e., third Gaussian) is scaled to a global minimum of -1, and the third well (i.e., fifth Gaussian) smoothly converges to zero at higher r values. This potential design is advantageous because the Gaussians can be changed intuitively: changing  $\epsilon_1$ ,  $\sigma_1$ , and  $\mu_1$ , for instance, changes the depth, width, and position of the first well, respectively. In

addition, the Yukawa potentials have a minimal effect on these parameter changes. We can easily change the well-depth parameters  $e_1$ ,  $e_2$ ,  $e_4$ , and  $e_5$ —the first four free parameters ( $e_3$  being scaled to -1)—in an intuitive manner. The other two free parameters are the well positions,  $\mu_3$  and  $\mu_5$ , which control the positions of the second and third wells, respectively ( $\mu_1$  is kept constant at r=1). All other parameters are coupled to the two well position parameters. Varying  $\mu_3$  by an arbitrary value,  $\delta$ , is reflected in the  $\mu_2$ ,  $\sigma_1$ , and  $\sigma_2$  terms where  $\mu_2$  is shifted by  $\delta/2$ ,  $\sigma_1 = (\mu_2 - \mu_1)^2$ , and  $\sigma_2 = [(\mu_3 - \mu_1)/2]^2$  to center the wells. Similarly, when varying  $\mu_5$ ,  $\mu_4$  is shifted by  $\delta/2$ ,  $\sigma_3 = [(\mu_4 - \mu_2)/2]^2$ ,  $\sigma_4 = [(\mu_5 - \mu_3)/2]^2$ , and  $\sigma_5 = (\mu_5 - \mu_4)^2$ . Boundary conditions for these parameters are shown in Figure 1d–f. These boundary conditions were set after initial testing to avoid singularities and strongly asymmetrical functional forms

To initiate the search for previously unknown self-assembled structures, we chose to survey the parameter space surrounding known, low-coordinated structures using our Y2G5P. Due to the flexibility and intuitiveness of our interaction potential design, we can easily fit the Y2G5P to other functional forms, for instance, the three-well OPP previously used to discover the first self-assembled icosahedral quasicrystal found in simulation. Whereas the OPP is only controlled by two parameters k and  $\phi$ —the oscillation's wavenumber and phase shift, respectively, which translate to changes in the shape of the oscillation in a nontrivial way—the Y2G5P can mimic the functional form of the OPP and can also access a higher-dimensional parameter space.

We fitted the Y2G5P to the shape of three-well OPPs that can simulate the self-assembly of the clathrate I structure type, cP54-K<sub>4</sub>Si<sub>23</sub> (see Figure 1c), and the clathrate II structure type cF160-Na<sub>24</sub>Si<sub>136</sub>. Structures are labeled using Pearson symbols, where the first letter indicates the crystal system and the second letter indicates the lattice centering type (together specifying the Bravais lattice), followed by the number of particles within a unit cell and the prototypical compound exhibiting such an arrangement of atoms. We use X to denote theoretical structures that have already been determined previously in the literature, <sup>14</sup> and we use  $\alpha$  and  $\beta$  to denote structures that, to our knowledge, had not been observed previously.

Table 1. Crystal Structures Observed by Surveying the Phase Space of Y2G5Ps<sup>a</sup>

Pearson symbol		Space group	CN	$\langle CN \rangle$	Comments
Known crystal structures					
cP54-K <sub>4</sub> Si <sub>23</sub>		$Pm\overline{3}n$	0/4	3.4	"clathrate I"
$cF160-Na_{24}Si_{136}$		$Fd\overline{3}m$	0/4	3.4	"clathrate II"
cI16-Si		$Ia\overline{3}$	4	4	high-pressure silicon
cI16- $X$		$Ia\overline{3}d$	5	5	simulated <sup>27</sup>
$tI4 ext{-Sn}$		$I4_1/amd$	6	6	A5 / "β-tin"
$cP4 ext{-Li}$		$P4_{1}32$	6	6	theoretical
hP1- $X$		P6/mmm	6	6	simulated <sup>14</sup>
hP2- $X$		$P6_3/mmc$	8	8	simulated $^{14,15}$
cF4-Cu		$Fm\overline{3}m$	12	12	A1 / ccp / "fcc"
$hP2 ext{-}\mathrm{Mg}$		$P6_3/mmc$	12	12	A3 / hcp
$cP$ 20- $\overline{\mathrm{Mn}}$		$P4_{1}32$	12/14	12.8	A13 / "β-Mn"
$hP7$ - $\operatorname{Zr}_4\operatorname{Al}_3$		P6/mmm	12/14/15	13.4	Frank-Kasper (FK) "Z" phase
$cP8$ - $Cr_3Si$		$Pm\overline{3}n$	12/14	13.5	A15 / FK phase
$cI2 ext{-W}$		$Im\overline{3}m$	$14^{'}$	14	A2 / "bcc"
Previously unknown low-coo	rdina	ted crystal stru	ıctures		·
$oI4$ - $\alpha$		Imma	2	2	
hR3- $lpha$		$R\overline{3}$	2	2	previously simulated under pressure 11
$mC32$ - $\alpha$		C2/c	2/3	2.5	
$hP47$ - $\alpha$		P6/mmm	0/2/4/5.5	3.4	similar to clathrate IV
$cI52$ - $\alpha$		$Im\overline{3}$	2/4	3.5	similar to clathrate I
$tI32$ - $\alpha$		$I4_1/acd$	3/4	3.5	
$hP44$ - $\alpha$		P6/mmm	0/4	3.6	clathrate IV with empty cages
cF144-Na <sub>8</sub> Si <sub>136</sub>		$Fd\overline{3}m$	0/4	3.7	clathrate II with empty cages
mC32- $eta$		C2/c	3/4/5	4	
$cP8$ - $\alpha$		$Pn\overline{3}m$	4	4	interconnected tetrahedra equivalent to $cF16$ -NaTl
$mC12$ - $\alpha$		C2/m	4/5	4.3	-
hP22- $lpha$		$P6_3/mcm$	4/5/6	4.9	
$tI16$ - $\alpha$		$I4_1/amd$	6/7	6.5	
$cI48$ - $\alpha$		$I\overline{4}3d$	7	7	
Previously unknown high-coe	ordin		uctures		
$hP3$ - $\alpha$		P6/mmm	11/14	12	
$mC16$ - $\alpha$		C2/m	10/13	12.3	
$oI24$ - $\alpha$		Imma	12/13/14	13	
$hP14$ - $\alpha$		P6/mcc	$13/14^{'}$	13.1	
$hP14$ - $\beta$		$P6_3/mmc$	12/14/15	13.4	$(1 \times 1 \times 2)$ -fold superstructure of $hP7$ - $Zr_4Al_3$
oI20- $lpha$		Imma	12/14/15	14	
Aperiodic crystal structures	and o	disorder	, ,		
previously unknown quasicrystal		_	_	_	
icosahedral quasicrystal		_	_	_	simulated $^{15}$
disorder		_	_	-	

<sup>&</sup>quot;Structures are split into four sections: known crystal structures, previously unknown low- and high-coordinated crystal structures, and aperiodic crystal structures and disorder. Within each section, structures are listed in order of their average coordination numbers, (CN).

Fitted Y2G5Ps are used as starting points to systematically explore the surrounding parameter space. The two clathrates were chosen for their complexity and low coordination numbers  $\langle \text{CN} \rangle \approx 4$ ; all clathrates contain particles that are 0- and 4-coordinated, with 0-coordinated particles located at the centers of cages formed by a network of tetrahedrally coordinated particles. While the clathrate IV structure type, hP47-X, has also been observed in simulation, <sup>15</sup> we were only able to isolate small grains from crystallized droplets where the majority phase was still either  $cP54-K_4Si_{23}$  or  $cF160-Na_{24}Si_{136}$ . We thus chose to exclude hP47-X as a starting point in our parameter space exploration. We also surveyed the parameter space surrounding  $tI32-\alpha$ , a structure found during our studies that possesses local environments of 3- and 4-coordinated particles.

#### **RESULTS**

We sample the parameter space surrounding cP54- $K_4Si_{23}$ , cF160- $Na_{24}Si_{136}$ , and tI32- $\alpha$  by taking two-dimensional cuts of the six-dimensional parameter space of Y2G5Ps, visualizing in

phase diagrams which self-assembled crystal structures are observed. We report the simulation of 20 previously unreported crystal structures, 14 of which are low-coordinated with local coordination numbers (CNs) ranging from 0 to 7, and 6 of which are high-coordinated with CNs ranging from 10 to 14. The CNs are determined using a crystal structure's radial distribution function (RDF), a histogram of the distances between pairs of particles, in which the first peak corresponds to the closest distances between particles. Particles that lie within a distance cutoff after the first peak in the RDF are considered to be within the first coordination shell. For clathrates, the first coordination shell denotes the tetrahedral network that forms the cages and excludes cage centers whose distances to neighboring network-forming particles are larger. We therefore consider these cage centers to be 0-coordinated. A visualization of previously unknown crystal structures is shown in Figure 2 and a list of all crystal structures, known and previously unknown, with their space groups, CNs, and average coordination numbers (CN) is shown in Table 1. Additional crystallographic information is detailed in the Supporting Information.

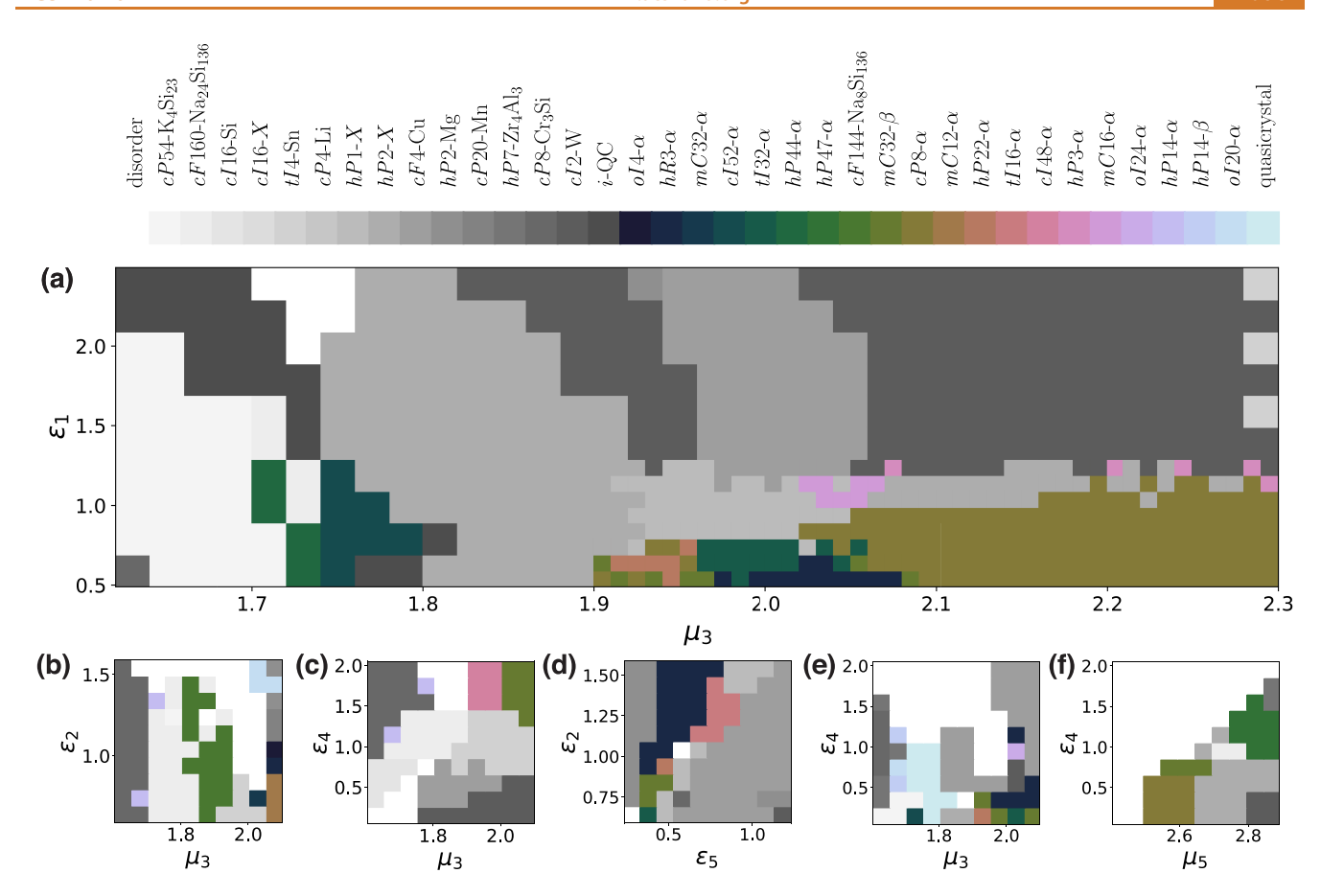


Figure 3. Phase diagrams surveying the parameter space surrounding cP54-K $_4$ Si $_2$ 3, cF160-Na $_2$ 4Si $_1$ 36, and tI32- $\alpha$  using Y2G5Ps. (a) Variation of the depth of the first well ( $\epsilon_1$ ) and position of the second well ( $\mu_3$ ) starting at cP54-K $_4$ Si $_2$ 3. (b,c) Variation of the height of the hump between the first and second wells ( $\epsilon_2$ ) and  $\mu_3$  and the height of the hump between the second and third wells ( $\epsilon_4$ ) and  $\mu_3$  starting at cF160-Na $_2$ 4Si $_1$ 36. (d-f) Variation of  $\epsilon_2$  and  $\epsilon_5$ ,  $\epsilon_4$  and  $\mu_3$ , and  $\epsilon_4$  and position of the third well ( $\mu_5$ ) starting at tI32- $\alpha$ . Previously unknown crystal structures are displayed in different colors, while known structures are shaded in gray.

All previously unknown crystal structures can be observed within the phase diagrams shown in Figure 3. Previously unknown crystal structures are displayed in different colors, while crystal structures that have been simulated previously are shaded in gray. While we investigated other regions of parameter space (reported in the Supporting Information), these regions yielded no additional structure types. Observed known crystal structures have local coordination numbers that range from 0 to 8 and from 12 to 15. Three of the known structures have been observed only in simulation and do not have atomic equivalents: cI16-X, hP1-X, and hP2-X. The cI16-X structure closely resembles that of cI16-Si, a high-pressure silicon phase, and has previously been observed in simulation using a harmonic-repulsive pair potential.<sup>27</sup> Both hP1-X and hP2-X were observed previously using LJGPs and OPPs.<sup>14,15</sup>

The largest explored phase diagram (see Figure 3a) surveys the parameter space surrounding cP54-K $_4$ Si $_{23}$  by varying the depth of the first well ( $\varepsilon_1$ ) and position of the second well ( $\mu_3$ ) of the Y2G5P. Increasing  $\varepsilon_1$  values correspond to a deeper first well, and increasing  $\mu_3$  values correspond to moving the position of the second well such that the distance between the first and second well increases. We ran a finer grid of state points at lower  $\varepsilon_1$  and higher  $\mu_3$  values, where we found the highest degree of structural diversity. A coarser grid was used for the rest of the phase diagram, which is dominated by known structures.

In total, the phase diagram consists of 650 individual state points with nine previously unknown crystal structures. Two of these previously unknown crystal structures,  $hP44-\alpha$  and  $cI52-\alpha$ , are found in the parameter space surrounded by two known clathrates cP54-K<sub>4</sub>Si<sub>23</sub> and cF160-Na<sub>24</sub>Si<sub>136</sub>, as well as an intermediate-density icosahedral quasicrystal, <sup>15</sup> and hP2-X. The  $hP44-\alpha$  structure has the same framework as hP47-X (clathrate IV; see Figure 4), with a unit cell containing three 20-vertex pentagonal dodecahedron-, two 24-vertex tetrakaidecahedron-, and two 26-vertex pentakaidecahedron-shaped cages. However, the  $hP44-\alpha$  structure is missing one set of cage centers at Wyckoff site 3f corresponding to the (smallest) cage centers of the pentagonal dodecahedron.

The  $cI52-\alpha$  structure bears a key similarity to the clathrate I structure type cP54- $K_4Si_{23}$ . Both structures contain two dodecahedron-shaped cages centered at (0,0,0) and (1/2,1/2,1/2) within their unit cells. Unlike cP54- $K_4Si_{23}$ , however, these cages are empty for  $cI52-\alpha$ . Additionally, whereas the cP54- $K_4Si_{23}$  unit cell contains another six tetrakaidodecahedron-shaped cages with cage centers,  $cI52-\alpha$  contains no additional cages. Instead, the dodecahedron-shaped cages are linked through 2-coordinated particles. As a result of these differences, the  $cI52-\alpha$  structure has space group  $Im\overline{3}$  with fewer symmetry elements than cP54- $K_4Si_{23}$ , which exhibits space group  $Pm\overline{3}n$ . These space groups are connected by space

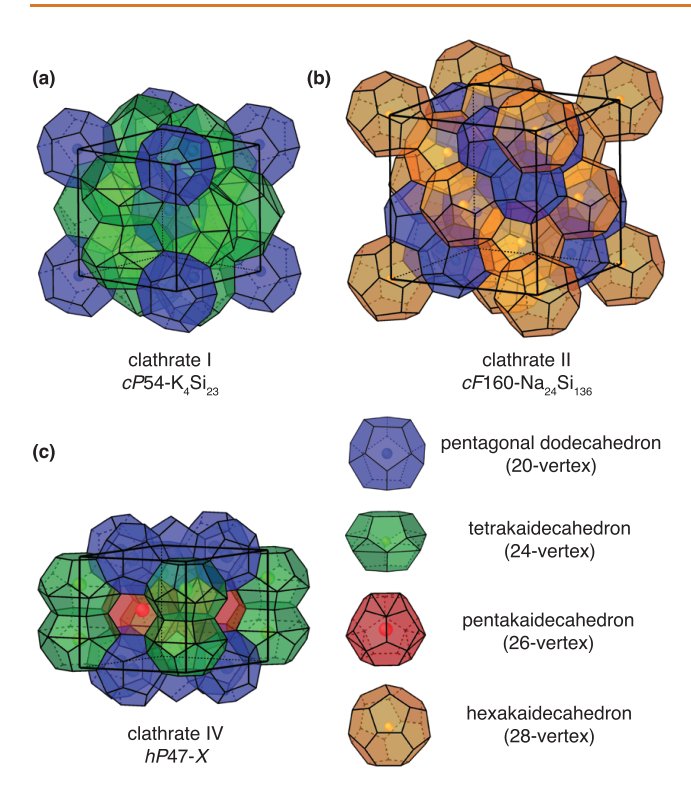


Figure 4. Unit cells of (a) clathrate I structure cP54-K<sub>4</sub>Si<sub>23</sub>, (b) clathrate II structure cF160-Na<sub>24</sub>Si<sub>136</sub>, and (c) clathrate IV structure hP47-X. Polyhedral cages, including the cage centers, are colored according to their respective shapes, shown on the bottom right.

group  $Pm\overline{3}$ , which is a maximal translationengleiche subgroup of  $Pm\overline{3}n$  and a maximal klassengleiche subgroup of  $Im\overline{3}$ .

The other seven previously unknown crystal structures found in the  $\epsilon_1 - \mu_3$  parameter space (Figure 3a) are clustered where the Y2G5P has a shallow first well (low  $\epsilon_1$  values) and larger spacing between the first and second well (high  $\mu_3$ values). Five of these structures— $hP22-\alpha$ ,  $hR3-\alpha$ ,  $mC32-\beta$ ,  $tI32-\alpha$ , and  $cP8-\alpha$ —are low-coordinated, and the other two  $hP3-\alpha$  and  $mC16-\alpha$ —are high-coordinated. The  $hP22-\alpha$ structure consists of a series of hexagonally linked distorted octahedra, forming flat layers that are stacked along the *c*-axis.  $hR3-\alpha$  is one of the lowest-coordinated structures found in this study and is a 2-coordinated columnar structure where particles are hexagonally arranged and have nearest neighbors only within these columns, arranged along the c-axis. This structure seems to correspond to another structure found in a previous computational study investigating the pressureinduced structures of a diamond-type phase. 11 Here, we find that the structure can be simulated without applying an elevated pressure.

We find similarities among the  $mC32-\beta$ ,  $tI32-\alpha$ , and  $cP8-\alpha$  structures, which all contain layers of tetrahedrally bonded particles. In the x-y plane, the  $mC32-\beta$  structure displays layers of tetrahedrally bonded particles that are alternated with layers of 3- and 5-coordinated particles. Similarly, the  $tI32-\alpha$  structure has layers of tetrahedrally bonded particles in the x-y plane, but these are separated by layers of 3-coordinated particles. Most of the low- $\epsilon_1$ -high- $\mu_3$  ("bottom right") region of the phase diagram is dominated by  $cP8-\alpha$ , which consists solely of AB-stacked layers of tetrahedra. The tetrahedra are interconnected equivalently to a double-diamond structure,

which in turn corresponds to *cF*16-NaTl (here, tetrahedra of two different orientations are located in the positions corresponding to Na and Tl).

The highly coordinated structures  $hP3-\alpha$  and  $mC16-\alpha$  border the large region of  $cP8-\alpha$ , as well as hP1-X, hP2-X, and cI2-W. The  $hP3-\alpha$  structure has high symmetry and consists of alternating layers of 11-coordinated polyhedra with 14-coordinated polyhedra, whereas the  $mC16-\alpha$  structure has low symmetry and consists of alternating layers of 10-coordinated polyhedra with 13-coordinated polyhedra.

Within the parameter space surrounding cF160-Na $_{24}$ Si $_{136}$ , seven additional previously unknown structures can be observed: cF144-Na $_8$ Si $_{136}$ , oI4- $\alpha$ , mC12- $\alpha$ , mC32- $\alpha$ , cI48- $\alpha$ , oI20- $\alpha$ , and hP14- $\alpha$  (Figure 3b,c). The cF144-Na $_8$ Si $_{136}$  structure has been observed experimentally and corresponds to the clathrate II structure cF160-Na $_{24}$ Si $_{136}$  (Figure 4) with missing cage centers. While both unit cells consist of 16 pentagonal dodecahedron- and 8 hexakaidecahedron-shaped cages, the cF144-Na $_8$ Si $_{136}$  structure is missing cage centers sitting within the pentagonal dodecahedra. This is in agreement with experimental studies where there is a preference for guest species to sit in the larger 28-vertex hexakaidecahedron rather than the smaller 20-vertex pentagonal dodecahedron.

Both the oI4- $\alpha$  and mC32- $\alpha$  structures have low symmetry and coordination numbers. The  $oI4-\alpha$  structure consists of buckled chains of 2-coordinated particles along the b-axis, whereas the  $mC32-\alpha$  structure forms a series of buckled chains along the c-axis that are also sometimes interconnected by 3coordinated particles. The  $mC12-\alpha$  structure is also low symmetry but consists of 4- and 5-coordinated particles. The  $cI48-\alpha$  structure has space group  $I\overline{4}3d$  and consists solely of 7coordinated particles sitting at Wyckoff position 48e. Both oI20- $\alpha$  and hP14- $\alpha$  structures have similarities with Frank-Kasper phases: the  $oI20-\alpha$  structure contains four 12coordinated, eight 14-coordinated, and eight 15-coordinated polyhedra in the unit cell but does not correspond to a Frank-Kasper phase,<sup>31</sup> and the  $hP14-\alpha$  structure consists of 14coordinated Frank-Kasper polyhedra but also contains 13coordinated polyhedra.

Within the parameter space surrounding tI32- $\alpha$ , another four periodic crystal structures can be observed (hP47- $\alpha$ , oI24- $\alpha$ , tI16- $\alpha$ , and hP14- $\beta$ ), as well as what appears to be a previously unknown quasicrystal structure (Figure 3d–f). hP47- $\alpha$  corresponds to hP47-X with half-occupied, off-center particles in the 20-vertex dodecahedron-shaped cages. These off-center cage centers are close enough to the framework to be located in the first neighbor shell of neighboring framework-building particles, which changes their coordination numbers from 0 and 4 to 2 and 5.5, respectively.

The  $oI24-\alpha$  structure consists of 12-, 13-, and 14-coordinated polyhedra but, similar to  $oI20-\alpha$ , does not correspond to a Frank–Kasper phase. The  $tI16-\alpha$  structure is composed of distorted flat hexagons that are linked in layers by 7-coordinated particles.  $hP14-\beta$  is a superstructure of  $hP7-Zr_4Al_3$ , with exactly double the number of 12-, 14-, and 15-coordinated polyhedra; however, the 12-coordinated polyhedra are distorted. Whereas  $hP7-Zr_4Al_3$  has space group P6/mmm,  $hP14-\alpha$  has space group  $P6_3/mmc$ , which is a maximal klassengleiche subgroup of index 2, with the unit cell parameter c'=2c.

The quasicrystal structure observed in the  $\epsilon_2$ – $\mu_3$  parameter space seems to be icosahedral, with characteristic 5-, 3-, and 2-

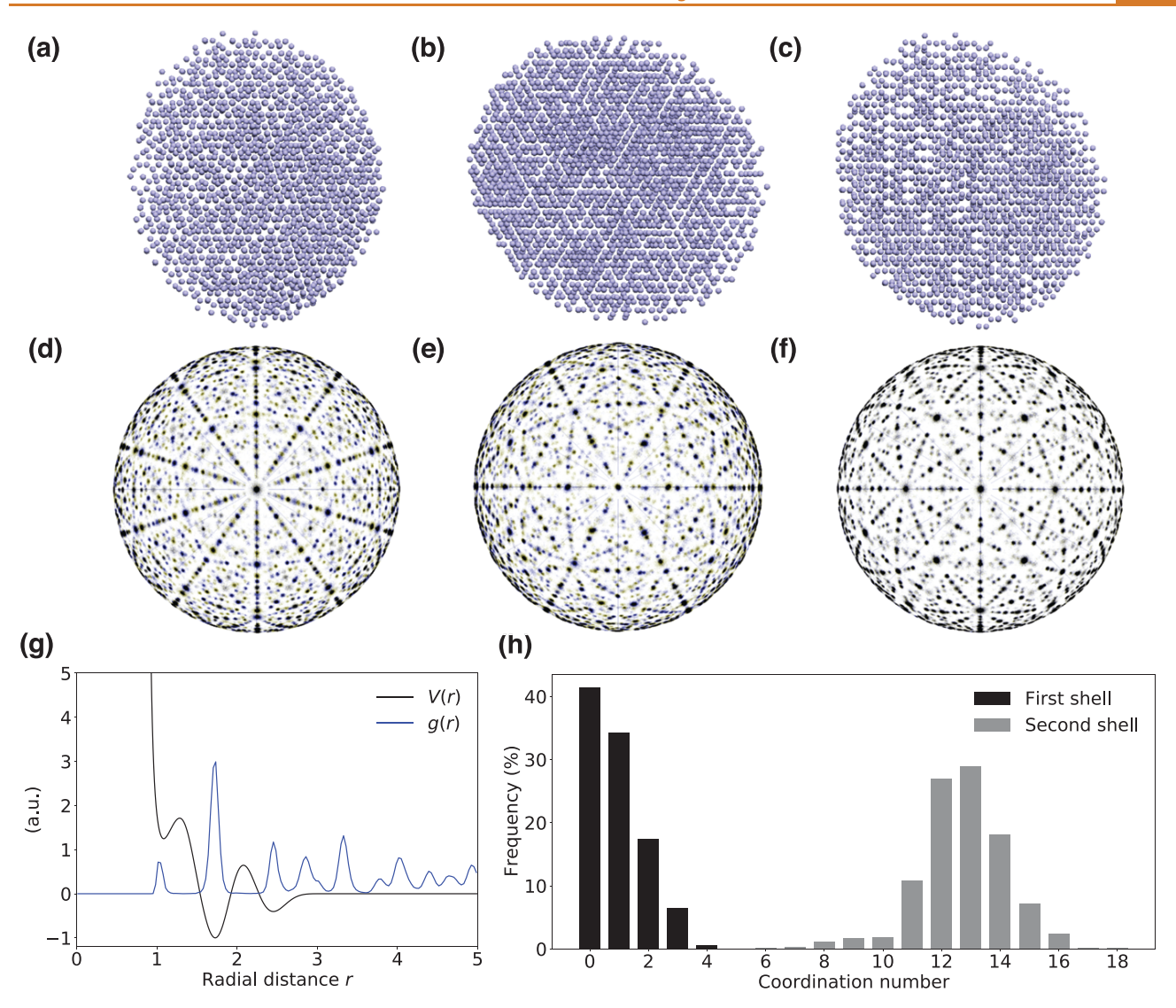


Figure 5. Self-assembled crystal structure that appears to be aperiodic. (a-c) Simulated crystallized droplets viewed along characteristic 5-, 3-, and 2-fold axes, respectively. (d-f) Corresponding bond-orientational order diagrams (BOODs), spherical projections of relative particle positions, along each of the main axes. (g) Crystal droplet's interaction potential (black) and corresponding RDF (blue). (h) Coordination numbers of the first (black) and second (gray) neighbor shells.

fold axes (Figure 5). The coordination number histogram (see Figure 5h) indicates that the first neighbor shell contains an  $\langle \text{CN} \rangle = 0.91$  with coordination numbers ranging from 0 to 4 and a second neighbor shell with  $\langle \text{CN} \rangle = 12.7$ . Within this plot, we correct for surface particles, which are missing nearest neighbors compared with bulk particles, in order to get an accurate representation of the quasicrystalline structure's coordination numbers. We remove surface particles within 3× the distance cutoff of the first neighbor shell determined using the RDF (here, we use a distance cutoff of 1.36) from consideration, thereby only counting the nearest neighbors of the bulk. Because the coordination environments differ from those reported in previous studies,  $^{15,32}$  we believe this to be a previously unknown quasicrystal. More in-depth structural analysis will be carried out in future work.

# **DISCUSSION**

In addition to finding previously unknown crystal structure types, our intuitively tunable Y2G5P design and systematic

searches in parameter space offer insight into the relation of the shape of the interaction potential to the resulting structure. Such relationships are necessary to determine the impact of specific features of the interaction potential on the selfassembly of various crystal structures and can lead to a predictive design. One quantifiable parameter that we investigated is the average number of nearest neighbors within the first neighbor shell per simulation state point. We replot the phase diagrams in Figure 3 by replacing state point labels related to the resulting structure with a color map representing the average coordination number (CN) extracted from the final frame of the simulated trajectory at each state point (see Figure 6). As detailed for the previously unknown quasicrystal, we remove surface particles from consideration in calculating the (CN) of the simulated droplets in order to obtain values that more accurately reflect the (CN) of the unit cell of each underlying structure. Similar analyses for other cuts through parameter space are reported in the Supporting Information.

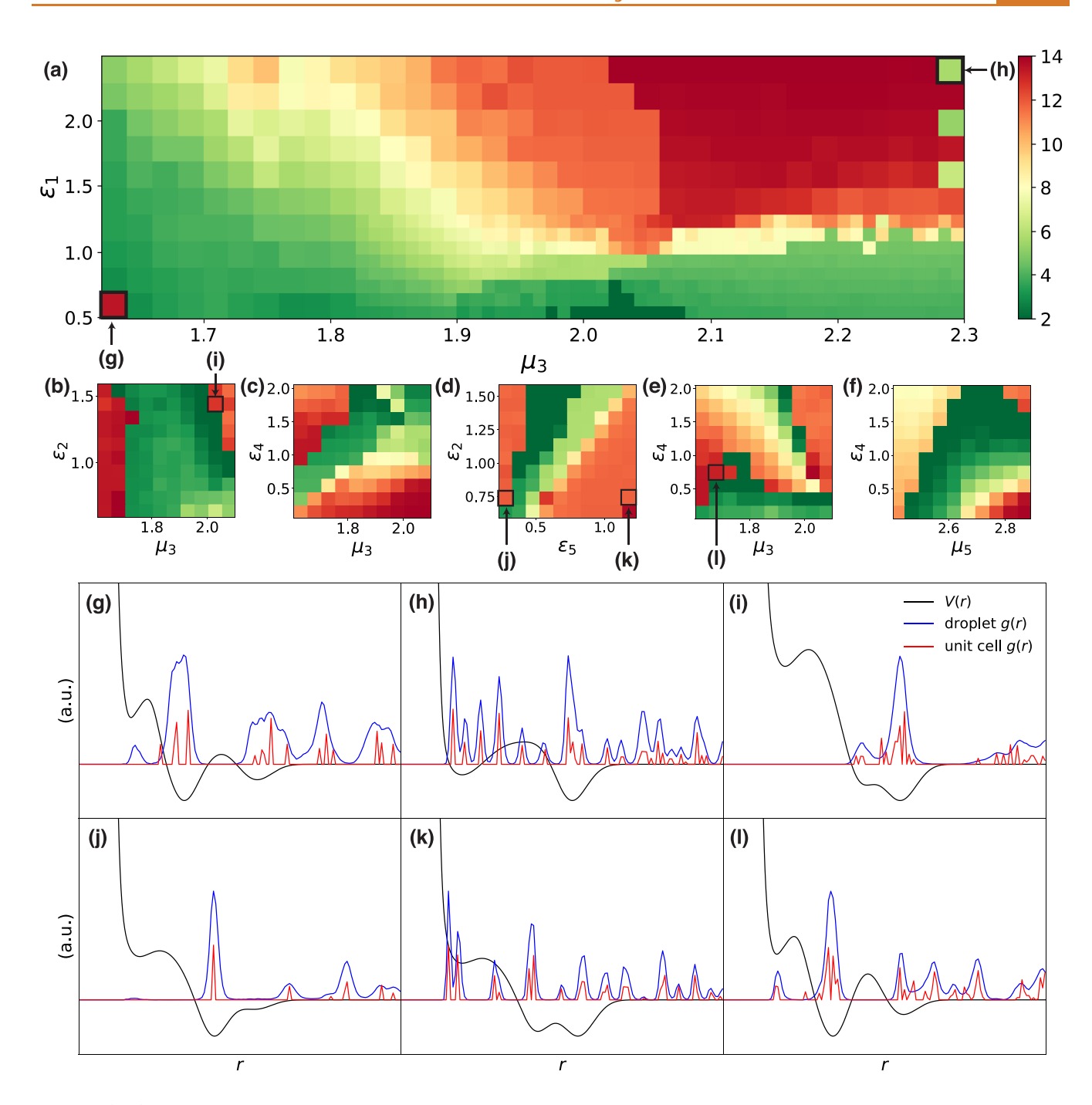


Figure 6. (a-f) Phase diagrams from Figure 3 where state points are now colored according to the average coordination number values  $\langle CN \rangle$  of simulated crystallized droplets. Low-, mid-, and high-coordinated structures are colored in shades of green, yellow, and red, respectively. (g-l) Interaction potentials (black) and RDFs of the simulated crystallized droplets (blue) and extracted unit cells (red) for selected state points.

The largest phase diagram shown in Figure 6 displays the most visible trend, where there is a fairly continuous transition from low- to high-coordinated structures (bottom middle to top right), which depends on both the depth of the first well and the position of the second well. As both parameters increase, the  $\langle \text{CN} \rangle$  value generally also increases. A few notable anomalies are located in the lower left corner, in which the majority of the resulting crystallite is  $cP8\text{-Cr}_3\text{Si}$  with a small grain of  $hP7\text{-Zr}_4\text{Al}_3$ , and in the upper right corner, where a few state points self-assemble into tI4-Sn. The corresponding

interaction potentials that self-assemble these structures, as well as the RDFs of the simulated droplet and extracted unit cell, are shown in Figures 6g—h. Both cases represent turning points where the definition of the RDF distance cutoff to determine nearest neighbors of the simulated droplet becomes ambiguous. For the simulation state point that self-assembles into mostly cP8- $Cr_3Si$ , the interaction potential has a sufficiently shallow first energy well (low  $\epsilon_1$  parameter value) such that very few particles sit within that distance, and most particles preferentially sit at a distance corresponding to the

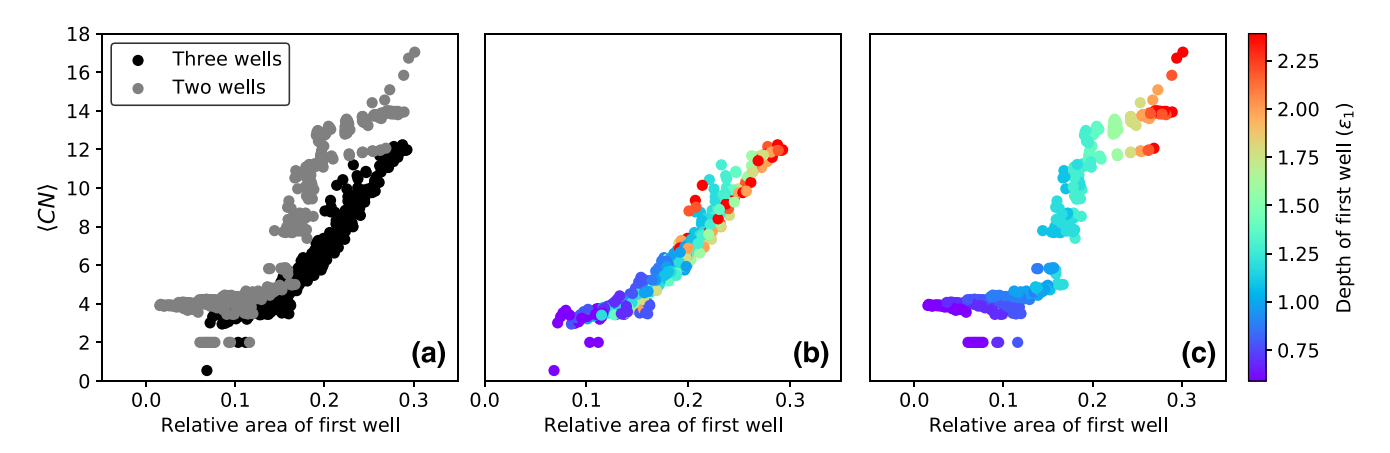


Figure 7. (a) Relationship between the relative area of the first well and the  $\langle CN \rangle$  of the resulting crystallized droplets when the depth of the first well  $(\epsilon_1)$  and the position of the second well  $(\mu_3)$  are tuned, colored by the number of wells of the underlying interaction potentials. (b) Relationship between the relative area of the first well and the  $\langle CN \rangle$  of the resulting crystallized droplet for three-well interaction potentials, colored by  $\epsilon_1$ . (c) Relationship between the relative area of the first well and the  $\langle CN \rangle$  for two-well interaction potentials, also colored by  $\epsilon_1$ .

ı

deep second energy well. In this case, the RDF of the full simulated droplet shows only a minor peak at the first energy well due to the close nearest neighbors of the small hP7-Zr<sub>4</sub>Al<sub>3</sub> grain. If we were to consider only nearest neighbors within a distance of this first peak, the (CN) value would be much lower ( $\sim$ 0.55), consistent with the low coordination numbers of surrounding state points. Similarly, the cutoff location for the first neighbor shell of tI4-Sn is generally ambiguous. The corresponding interaction potential has a deep and wide first energy well (high  $\epsilon_1$  parameter value), stimulating the formation of highly coordinated structures, and the position of the second well has been tuned so far such that it merges with the third energy well. Many particle-particle distances of the tI4-Sn structure fall within the first energy well; however, the small variations in particle-particle distances (multiple peaks) contribute to an ambiguous RDF distance cutoff. While we use the distance after the first staggered peak to calculate the (CN) value, (CN) would be considerably higher, consistent with the high coordination numbers of surrounding state points, had we chosen a larger distance cutoff value.

In other cuts through the parameter space, differing trends emerge. Changing the  $\epsilon_2$  and  $\mu_3$  parameters in the parameter space surrounding cF160-Na<sub>24</sub>Si<sub>136</sub>, for instance, results in  $\langle CN \rangle$  values that seem to depend more on the  $\mu_3$  parameter (see Figure 6b). At low  $\mu_3$  values, high-coordinated cP8-Cr<sub>3</sub>Si dominates across all  $\epsilon_2$  values, in which the first-shell particle particle distances lie within the second energy well. As  $\mu_3$  is increased, increasing the distance between the first and second wells of the interaction potential, a sharp transition to lowcoordinated structures occurs, as it seemingly becomes more favorable for particles to sit in the first energy well. At high  $\epsilon_2$ and  $\mu_3$  values, we observe a transition back to high-coordinated structures, namely,  $oI20-\alpha$ , cP20-Mn, and hP2-Mg. For these structures, the particles again sit at a distance corresponding to the second energy well, most likely due to the high  $\epsilon_2$ parameter, which enforces a high barrier between the first and second wells of the interaction potential. An example of the interaction potential and RDFs of the simulated droplet and extracted unit cell of an  $oI20-\alpha$ -forming state point is shown in Figure 6i.

A similar and interesting progression appears as we vary the  $\epsilon_2$  and  $\epsilon_5$  parameters surrounding the  $tI32-\alpha$  structure (Figure 6d). Within this phase diagram, we observe two versions of the

*hP2-Mg* structure: one in which the interparticle distances correspond to the second energy well (Figure 6j) and another in which the interparticle distances correspond to the first energy well (Figure 6k). Curiously, this effect can occur by tuning the  $\epsilon_5$  parameter, which changes the depth of the third well of the interaction potential. Thus, while it may seem intuitive that changing the features at lower interparticle distances would have the most impact on the resulting self-assembled crystal structure, we still find differences in  $\langle \text{CN} \rangle$  value as well as structural diversity when tuning features at higher interparticle distances. This observation is further exemplified in Figure 6f, where the  $\langle \text{CN} \rangle$  value changes when only  $\epsilon_4$  and  $\epsilon_5$  parameters are varied, even resulting in several previously unknown crystal structure types.

In general, we find that it is difficult to identify trends between the parameters controlling the features of the interaction potential and the (CN) value. In most cuts through parameter space, the (CN) depends on both parameters, suggesting that the resulting structures depend on the shape of the interaction potential as a whole rather than on individual features. A further exemplification of this is shown in Figure 6c,e, in which tuning the same parameters ( $\epsilon_4$ and  $\mu_3$ ) but with different starting interaction potential shapes results in contrasting heatmaps. Additionally, while we specifically targeted the self-assembly of low-coordinated structures by enforcing a first repulsive well, we observed high-coordinated structures within every cut through parameter space. High-coordinated structures typically emerge when there is a deep and sufficiently wide first well, or otherwise a sufficiently shallow first well, so that particles preferentially sit at the second energy well. Intriguingly, while simulated droplets with intermediate (CN) values are also ubiquitous, these droplets are mainly disordered or else form  $hP1-\alpha$  or  $hP2-\alpha$ , and we find no additional previously unknown crystal structure types with intermediate coordination numbers. We do, however, observe "intermediate"-type structures such as  $oI24-\alpha$  (Figure 6l), where the first neighbor shell includes mostly interparticle distances at the second energy well but also a few interparticle distances at the first energy well, still a physically meaningful distance away from neighboring particles. Such structures typically occur between sharp transitions from low- to high-coordinated regions of parameter space.

While generalizations across parameter space are difficult, we observe predictive trends between the relative areas of the wells and humps, which are normalized by the total area of the interaction potential features, and the (CN) of the resulting crystallized droplets. Here, we use the position of the hump maximum between the first and second wells  $(\mu_2)$  as the radial cutoff value to determine (CN). Figure 7a illustrates the relationship between the relative area of the first well and the (CN) as we tune the depth of the first well and the position of the second well within the largest cut through parameter space that we examined. We observe that the relative area of the netrepulsive first well is linearly correlated with the (CN) when the interaction potential possesses three wells (black): the smallest relative areas of the first well correspond to low  $\langle CN \rangle$ values. When colored by the depth of the first well  $(\epsilon_1)$ , as shown in Figure 7b, it becomes clear that the width of the first well, which is tied to the position of the second well  $(\mu_3)$ , plays a critical role in determining the range of (CN) values that the resulting structures adopt. At the lowest  $\epsilon_1$  value (purple), corresponding to a small well depth, there is a limited range of relative areas of the first well as  $\mu_3$  is increased and the lowest (CN) values (less than 4) are achieved. With each successively deeper first well, the range of (CN) values is expanded. At the highest  $\epsilon_1$  value (red),  $\langle CN \rangle$  values as low as 5.1 and as high as 12 are observed as the relative area of the first well is increased. Thus, in the case of three-well interaction potentials, a netrepulsive first well with a small relative area can enforce low coordination; however, low coordination can still be achieved with slightly larger relative areas given a narrow, deep first well.

The relative area of the first well is also predictive of the (CN) when the interaction potential possesses two wells (gray), as shown in Figure 7a. The two-well interaction potentials, which occur once the position of the second well is tuned so far that it merges with the third well, appear to follow an S-shaped curve rather than a linear trend, which the threewell interaction potentials exhibit (Figure 7c). The smaller relative areas of the first well (0.0 to 0.15) are associated with low (CN) values, high relative areas (0.2 to 0.3) are associated with high (CN) values, and the transition from low to high coordination occurs steeply in between (with relative areas ranging from 0.15 to 0.2). This predictive trend appears to be strongly related to the parameter values of the depth of the first well  $(\epsilon_1)$ , where a shallow first well corresponds to low  $\langle CN \rangle$ values and smaller relative areas of the first well and a deep first well corresponds to high (CN) values and larger relative areas of the first well. Depictions of corresponding example interaction potential shapes can be found in the Supporting Information.

# **CONCLUSION**

The previously unknown crystal structures reported here represent a taste of the potentially infinite undiscovered and exotic configurations of materials possible through self-assembly with controlled particle interactions. Several of the previously unknown structures we reported have local environments that are rare on the atomic scale, for instance the 2-coordinated environments present in  $oI4-\alpha$ ,  $hR3-\alpha$ ,  $mC32-\alpha$ , and  $cI52-\alpha$ , as well as the atypical 11- and 13-coordinated environments present in  $hP3-\alpha$ ,  $mC16-\beta$ ,  $oI24-\alpha$ , and  $hP14-\alpha$ . We also observe previously unknown structures with low symmetry, namely,  $mC32-\alpha$ ,  $mC32-\beta$ ,  $mC12-\alpha$  and  $mC16-\alpha$ . Such low-symmetry structures, while seemingly ubiquitous in experiments (approximately 20% of the entries

in ICSD report structures with space groups no. 15 or lower), go beyond those previously achieved in self-assembly simulations.<sup>33</sup>

The search for undiscovered materials hinges on our knowledge of the exact interactions that enable the selfassembly of different crystal structures, and thus, an understanding of how individual features can impact the resulting structure is useful to both computationalists and experimentalists in establishing design rules and guiding future studies. We push the boundaries of this area of research by intentionally designing a versatile and intuitively tunable isotropic particle pair potential—the Y2G5P. By relating the parameters controlling the individual features of the interaction potential to the resulting crystal droplets (CN), however, we observe a complicated relationship. This may partially be due to the vast parameter space, whose exploration we have begun to attempt with investigating dedicated regions and lowdimensional sweeps rather than a random sampling of the full search space. We find that the relative areas of the interaction potential wells and humps is a more predictive measure for (CN), in which trends can be further teased apart by the number of wells and parameter values that control the shape of the interaction potential. We show that low (CN) values can be enforced by small relative areas of the first well for both two- and three-well interaction potentials. We also uncover two differing predictive trends: a linear relationship between (CN) values and the relative area of the first well when the interaction potential possesses three wells and an S-shaped interdependence when the interaction potential possesses two wells. Such trends, however, are less conclusive when applied to a variety of interaction potential shapes.

We have shown that by narrowing our search to target low-coordinated structures, we observe a number of previously unknown crystal structure types by sampling the parameter space surrounding known low-coordinated assemblies. Yet, we did not observe such structures as diamond, which was previously observed using a similar pair potential, <sup>24</sup> or the 3-coordinated gyroid structure type, which should be realistic target structures with our interaction potential ansatz. Such gaps suggest that there are many more crystal structure configurations yet to be explored in the realm of isotropic pair potentials, which leaves exciting areas to investigate in future work.

Finally, we emphasize that these pair potentials program particles using effective interactions with multiple competing length scales, a proxy for the complex interplay between a variety of interactions from, e.g., solvents or charge. Our current study can therefore be viewed as an abstract approach to exploring the theoretical parameter space of such systems. While recreating pair interactions in experiments that exactly correspond to multiwell potentials is currently challenging, studies have already begun to establish the connection between pair interactions in experiments and their effective pair potentials in systems of DNA-functionalized colloids,<sup>34</sup> polymer-functionalized nanoparticles<sup>35,36</sup> and star polymers.<sup>37–39</sup> Some studies have even disentangled the competing interactions that result in the shape of effective interaction potentials with multiple features. 40 Additionally, several inverse design approaches that optimize thermodynamic properties 41,42 such as energy 23,24 or relative entropy, 43-45 have been developed to target simpler interaction potentials given prior knowledge of the crystal structure. While in the present work we use forward design in order to uncover the

ACS Nano www.acsnano.org Article

interactions that will assemble unexpected crystal structure configurations, inverse design may be a key step in turning these interaction potentials into a form that is easier to recreate in experiments.

#### **METHODS**

Self-assembly molecular dynamics (MD) simulations are carried out using HOOMD-blue, a versatile open-source simulation package.  $^{46-48}$  Systems containing N=4096 particles are initialized in the gas phase at high temperature and are linearly cooled in the NVT ensemble using the Nosé–Hoover thermostat over the course of  $10^8$  time steps with step size  $d\tau=0.005$ . Particles are initialized on a regular grid at large interparticle distances and, due to the high starting temperature, are automatically randomized within the first several MD steps. Upon cooling, the particles condense into a liquid droplet and later solidify spontaneously, usually ordering into a crystalline assembly. We visualize the simulation trajectories using  $plato,^{49}$  perform structural analysis using  $freud,^{50}$  and use  $signac^{51,52}$  for data and workflow management.

Crystal structures formed by particles in simulations are characterized by first extracting the unit cell from the final frame of simulation trajectories. We start by isolating a single grain since the majority of the simulations do not result in single crystals. We then plot the radial distribution functions (RDFs), which map the density of neighboring particles from a central particle across different radial distances, in order to determine the numbers of nearest neighbors, which often unambiguously correspond to a distance cutoff after the first peak. Bond-orientational order diagrams (BOODs), which project all particle positions relative to each other onto a sphere in a global coordinate system, are used to determine the orientation of the main directions of the crystal. We then use cylindrical BOODs, which map the frequency of particle distances along the main directions determined in the previous step, to determine periodicity, i.e., the unit cell dimensions. The vectors that are extracted are used to cluster particle positions in a unit cell, and we use Spglib<sup>53</sup> to determine the space group and thus the Wyckoff sites of the particle positions in the resulting unit cell. We confirm that the crystal structures reported here have not been observed previously by comparing our simulation results to reported structures in the Inorganic Crystal Structure Database.54

# **ASSOCIATED CONTENT**

# **5** Supporting Information

The Supporting Information is available free of charge at https://pubs.acs.org/doi/10.1021/acsnano.2c09131.

Additional crystallographic data and figures of the previously unknown structures self-assembled in this study, as well as example interaction potential shapes and corresponding RDFs and BOODs; a table of parameter values for all sampled state points; phase diagrams and  $\langle \text{CN} \rangle$  heatmaps of sampled state points not reported in the main text; and example interaction potentials describing the relation between relative areas of interaction potential features and the assembled crystal structure's  $\langle \text{CN} \rangle$  (PDF)

# **AUTHOR INFORMATION**

#### **Corresponding Author**

Julia Dshemuchadse — Department of Materials Science and Engineering, Cornell University, Ithaca, New York 14853, United States; orcid.org/0000-0003-2310-6687; Email: jd732@cornell.edu

#### **Author**

Hillary Pan — Department of Materials Science and Engineering, Cornell University, Ithaca, New York 14853, United States; Occid.org/0000-0002-4073-2180

Complete contact information is available at: https://pubs.acs.org/10.1021/acsnano.2c09131

#### Note

The authors declare no competing financial interest.

Citation Diversity Statement. Recent work in several fields of science has identified a bias in citation practices such that papers from women and other minority scholars are undercited relative to the number of such papers in the field (e.g., refs 56-58). In order to begin to provide transparency and accountability for citation gender imbalance, 59 we used an open-source code that predicts the gender of the first and last author of each reference by using databases that store the probability of a first name being carried by a woman. 57,60 Much to our regret, this method cannot account for intersex, nonbinary, or transgender people. Excluding self-citations, our references contain 8.29% woman(first)/woman(last), 22.64% man/woman, 9.38% woman/man, and 59.69% man/ man by this measure. (This method is limited in that names, pronouns, and social media profiles used to construct the databases may not, in every case, be indicative of gender identity.)

#### **ACKNOWLEDGMENTS**

This work was supported by the Cornell Center for Materials Research with funding from the NSF MRSEC program (DMR-1719875). This work was performed at the Cornell University Center for Advanced Computing (CAC), at the Cornell NanoScale Facility—a member of the National Nanotechnology Coordinated Infrastructure (NNCI), which is supported by the National Science Foundation (Grant No. ECCS-2025233)—and this work used the Extreme Science and Engineering Discovery Environment (XSEDE),55 which is supported by National Science Foundation grant number ACI-1548562; XSEDE award DMR-190048. We would like to thank Matthew Spellings and Vyas Ramasubramani for contributions to the computational crystal structure analysis pipeline. We would also like to thank Jasmin J. Kennard, Maya M. Martirossyan, and Rachael S. Skye for helpful discussions and feedback.

#### REFERENCES

- (1) Kim, S. A.; Jeong, K.; Yethiraj, A.; Mahanthappa, M. K. Low-symmetry sphere packings of simple surfactant micelles induced by ionic sphericity. *Proc. Natl. Acad. Sci. U. S. A.* **2017**, *114*, 4072–4077.
- (2) Zeng, X.; Ungar, G.; Liu, Y.; Percec, V.; Dulcey, A. E.; Hobbs, J. K. Supramolecular dendritic liquid quasicrystals. *Nature* **2004**, *428*, 157–160.
- (3) Ungar, G.; Zeng, X. Frank-Kasper, quasicrystalline and related phases in liquid crystals. *Soft Matter* **2005**, *1*, 95–106.
- (4) Lee, S.; Leighton, C.; Bates, F. S. Sphericity and symmetry breaking in the formation of Frank-Kasper phases from one component materials. *Proc. Natl. Acad. Sci. U. S. A.* **2014**, *111*, 17723–17731.
- (5) Chanpuriya, S.; Kim, K.; Zhang, J.; Lee, S.; Arora, A.; Dorfman, K. D.; Delaney, K. T.; Fredrickson, G. H.; Bates, F. S. Cornucopia of Nanoscale Ordered Phases in Sphere-Forming Tetrablock Terpolymers. ACS Nano 2016, 10, 4961–4972.

- (6) Hajiw, S.; Pansu, B.; Sadoc, J.-F. Evidence for a C14 Frank–Kasper Phase in One-Size Gold Nanoparticle Superlattices. *ACS Nano* **2015**, *9*, 8116–8121.
- (7) Glotzer, S. C.; Solomon, M. J. Anisotropy of building blocks and their assembly into complex structures. *Nat. Mater.* **2007**, *6*, 557–562.
- (8) Lin, H.; Lee, S.; Sun, L.; Spellings, M.; Engel, M.; Glotzer, S. C.; Mirkin, C. A. Clathrate colloidal crystals. *Science* **2017**, 355, 931–935.
- (9) He, M.; Gales, J. P.; Ducrot, E.; Gong, Z.; Yi, G.; Sacanna, S.; Pine, D. J. Colloidal Diamond. *Nature* **2020**, *585*, 524–529.
- (10) Ducrot, É.; He, M.; Yi, G.; Pine, D. J. Colloidal alloys with preassembled clusters and spheres. *Nat. Mater.* **2017**, *16*, 652–657.
- (11) Bertolazzo, A. A.; Kumar, A.; Chakravarty, C.; Molinero, V. Water-like Anomalies and Phase Behavior of a Pair Potential that Stabilizes Diamond. *J. Phys. Chem. B* **2016**, 120, 1649–1659.
- (12) Travesset, A. Phase diagram of power law and Lennard-Jones systems: Crystal phases. J. Chem. Phys. 2014, 141, 164501.
- (13) Jones, J. E. On the determination of molecular fields.—II. From the equation of state of a gas. *Proc. R. Soc. London A* **1924**, *106*, 463–477.
- (14) Dshemuchadse, J.; Damasceno, P. F.; Phillips, C. L.; Engel, M.; Glotzer, S. C. Moving beyond the constraints of chemistry via crystal structure discovery with isotropic multiwell pair potentials. *Proc. Natl. Acad. Sci. U. S. A.* **2021**, *118*, e2024034118.
- (15) Engel, M.; Damasceno, P. F.; Phillips, C. L.; Glotzer, S. C. Computational self-assembly of a one-component icosahedral quasicrystal. *Nat. Mater.* **2015**, *14*, 109–116.
- (16) Ranocchiari, M.; van Bokhoven, J. A. Catalysis by metal-organic frameworks: fundamentals and opportunities. *Phys. Chem. Chem. Phys.* **2011**, *13*, 6388.
- (17) Babucci, M.; Guntida, A.; Gates, B. C. Atomically Dispersed Metals on Well-Defined Supports including Zeolites and Metal-Organic Frameworks: Structure, Bonding, Reactivity, and Catalysis. *Chem. Rev.* **2020**, *120*, 11956–11985.
- (18) Zhao, Y.; Shang, L.; Cheng, Y.; Gu, Z. Spherical Colloidal Photonic Crystals. Acc. Chem. Res. 2014, 47, 3632–3642.
- (19) Ho, K. M.; Chan, C. T.; Soukoulis, C. M. Existence of a photonic gap in periodic dielectric structures. *Phys. Rev. Lett.* **1990**, 65, 3152–3155.
- (20) Stillinger, F. H.; Weber, T. A. Computer simulation of local order in condensed phases of silicon. *Phys. Rev. B* **1985**, *31*, 5262–5271
- (21) Molinero, V.; Moore, E. B. Water Modeled as an Intermediate Element between Carbon and Silicon. *J. Phys. Chem. B* **2009**, *113*, 4008–4016.
- (22) Cisneros, G. A.; Wikfeldt, K. T.; Ojamäe, L.; Lu, J.; Xu, Y.; Torabifard, H.; Bartók, A. P.; Csányi, G.; Molinero, V.; Paesani, F. Modeling Molecular Interactions in Water: From Pairwise to Many-Body Potential Energy Functions. *Chem. Rev.* **2016**, *116*, 7501–7528.
- (23) Rechtsman, M. C.; Stillinger, F. H.; Torquato, S. Self-assembly of the simple cubic lattice with an isotropic potential. *Phys. Rev. E* **2006**, 74, 021404.
- (24) Rechtsman, M. C.; Stillinger, F. H.; Torquato, S. Synthetic diamond and wurtzite structures self-assemble with isotropic pair interactions. *Phys. Rev. E* **2007**, *75*, 031303.
- (25) Cersonsky, R. K.; Antonaglia, J.; Dice, B. D.; Glotzer, S. C. The diversity of three-dimensional photonic crystals. *Nat. Commun.* **2021**, 12, 2543.
- (26) Yukawa, H. On the interaction of elementary particles. *Proc. Phys. Math. Soc. Japan* **1935**, *17*, 48–57.
- (27) Lokshin, K. A.; Levashov, V. A.; Lobanov, M. V. A new cubic  $Ia\overline{3}d$  crystal structure observed in a model single component system by molecular dynamics simulation. *Z. Kristallogr. Cryst. Mater.* **2018**, 233, 67–71.
- (28) Beekman, M.; Nenghabi, E. N.; Biswas, K.; Myles, C. W.; Baitinger, M.; Grin, Y.; Nolas, G. S. Framework Contraction in Na-Stuffed Si(cF136). *Inorg. Chem.* **2010**, *49*, 5338–5340.
- (29) Stefanoski, S.; Malliakas, C. D.; Kanatzidis, M. G.; Nolas, G. S. Synthesis and Structural Characterization of  $Na_xSi_{136}$  (0 <  $x \le 24$ )

- Single Crystals and Low-Temperature Transport of Polycrystalline Specimens. *Inorg. Chem.* **2012**, *51*, 8686–8692.
- (30) Sloan, E. D., Jr. Clathrate Hydrates of Natural Gases; Marcel Dekker, Inc.: New York, 1998.
- (31) Sikirić, M. D.; Delgado-Friedrichs, O.; Deza, M. Space fullerenes: a computer search for new Frank-Kasper structures. *Acta Crystallogr. A* **2010**, *66*, 602–615.
- (32) Damasceno, P. F.; Glotzer, S. C.; Engel, M. Non-close-packed three-dimensional quasicrystals. *J. Phys.: Condens. Matter* **2017**, 29, 234005.
- (33) Dshemuchadse, J. Soft matter crystallography—Complex, diverse, and new crystal structures in condensed materials on the mesoscale. *J. Appl. Phys.* **2022**, *131*, 020901.
- (34) Rogers, W. B.; Crocker, J. C. Direct measurements of DNA—mediated colloidal interactions and their quantitative modeling. *Proc. Natl. Acad. Sci. U.S.A.* **2011**, *108*, 15687–15692.
- (35) Khan, S. J.; Pierce, F.; Sorensen, C. M.; Chakrabarti, A. Self-Assembly of Ligated Gold Nanoparticles: Phenomenological Modeling and Computer Simulations. *Langmuir* **2009**, *25*, 13861–13868.
- (36) Schapotschnikow, P.; Pool, R.; Vlugt, T. J. A. Molecular Simulations of Interacting Nanocrystals. *Nano Lett.* **2008**, *8*, 2930–2934
- (37) Likos, C. N.; Löwen, H.; Watzlawek, M.; Abbas, B.; Jucknischke, O.; Allgaier, J.; Richter, D. Star Polymers Viewed as Ultrasoft Colloidal Particles. *Phys. Rev. Lett.* **1998**, *80*, 4450–4453.
- (38) Likos, C. N. Effective interactions in soft condensed matter physics. *Phys. Rep.* **2001**, 348, 267–439.
- (39) Likos, C. N.; Hoffmann, N.; Löwen, H.; Louis, A. A. Exotic fluids and crystals of soft polymeric colloids. *J. Phys.: Condens. Matter* **2002**, *14*, 7681–7698.
- (40) Van Lehn, R. C.; Alexander-Katz, A. Ligand-Mediated Short-Range Attraction Drives Aggregation of Charged Monolayer-Protected Gold Nanoparticles. *Langmuir* **2013**, *29*, 8788–8798.
- (41) van Anders, G.; Klotsa, D.; Karas, A. S.; Dodd, P. M.; Glotzer, S. C. Digital Alchemy for Materials Design: Colloids and Beyond. *ACS Nano* **2015**, *9*, 9542–9553.
- (42) Zhou, P.; Glotzer, S. C. Inverse design of isotropic pair potentials using digital alchemy with a generalized Fourier potential. *Eur. Phys. J. B* **2021**, *94*, 243.
- (43) Jain, A.; Errington, J. R.; Truskett, T. M. Inverse design of simple pairwise interactions with low-coordinated 3D lattice ground states. *Soft Matter* **2013**, *9*, 3866.
- (44) Jadrich, R. B.; Lindquist, B. A.; Truskett, T. M. Probabilistic inverse design for self-assembling materials. *J. Chem. Phys.* **2017**, *146*, 184103.
- (45) Adorf, C. S.; Antonaglia, J.; Dshemuchadse, J.; Glotzer, S. C. Inverse design of simple pair potentials for the self-assembly of complex structures. *J. Chem. Phys.* **2018**, *149*, 204102.
- (46) Anderson, J. A.; Lorenz, C. D.; Travesset, A. General purpose molecular dynamics simulations fully implemented on graphics processing units. *J. Comput. Phys.* **2008**, 227, 5342–5359.
- (47) Glaser, J.; Nguyen, T. D.; Anderson, J. A.; Lui, P.; Spiga, F.; Millan, J. A.; Morse, D. C.; Glotzer, S. C. Strong scaling of general-purpose molecular dynamics simulations on GPUs. *Comput. Phys. Commun.* **2015**, 192, 97–107.
- (48) Anderson, J. A.; Glaser, J.; Glotzer, S. C. HOOMD-blue: A Python package for high-performance molecular dynamics and hard particle Monte Carlo simulations. *Comput. Mater. Sci.* **2020**, *173*, 109363.
- (49) Plato; https://plato-draw.readthedocs.io/ (accessed on February 1, 2023).
- (50) Dice, B. D.; Ramasubramani, V.; Harper, E. S.; Spellings, M. P.; Anderson, J. A.; Glotzer, S. C. Analyzing Particle Systems for Machine Learning and Data Visualization with freud. *Proceedings of the 18th Python in Science Conference* **2019**, 27–33.
- (51) Adorf, C. S.; Dodd, P. M.; Ramasubramani, V.; Glotzer, S. C. Simple data and workflow management with the signac framework. *Comput. Mater. Sci.* **2018**, *146*, 220–229.

- (52) Ramasubramani, V.; Dice, B. D.; Harper, E. S.; Spellings, M. P.; Anderson, J. A.; Glotzer, S. C. freud: A Software Suite for High Throughput Analysis of Particle Simulation Data. Comput. Phys. Commun. 2020, 254, 107275.
- (53) Togo, A.; Tanaka, I. Spglib: a software library for crystal symmetry search. arXiv 2018; https://arxiv.org/abs/1808.01590 (accessed on February 1, 2023).
- (54) FIZ Karlsruhe, Inorganic Crystal Structure Database—ICSD; https://icsd.fiz-karlsruhe.de (accessed on February 1, 2023).
- (55) Towns, J.; Cockerill, T.; Dahan, M.; Foster, I.; Gaither, K.; Grimshaw, A.; Hazlewood, V.; Lathrop, S.; Lifka, D.; Peterson, G. D.; Roskies, R.; Scott, J. R.; Wilkins-Diehr, N. XSEDE: Accelerating Scientific Discovery. Computing in Science & Engineering 2014, 16, 62 - 74.
- (56) Caplar, N.; Tacchella, S.; Birrer, S. Quantitative evaluation of gender bias in astronomical publications from citation counts. Nature Astronomy 2017, 1, 0141.
- (57) Dworkin, J. D.; Linn, K. A.; Teich, E. G.; Zurn, P.; Shinohara, R. T.; Bassett, D. S. The extent and drivers of gender imbalance in neuroscience reference lists. Nature Neuroscience 2020, 23, 918-926.
- (58) Chatterjee, P.; Werner, R. M. Gender Disparity in Citations in High-Impact Journal Articles. JAMA Netw. Open 2021, 4, e2114509.
- (59) Dworkin, J.; Zurn, P.; Bassett, D. S. (In)citing Action to Realize an Equitable Future. Neuron 2020, 106, 890-894.
- (60) Zhou, D.; Cornblath, E. J.; Stiso, J.; Teich, E. G.; Dworkin, J. D.; Blevins, A. S.; Bassett, D. S. Gender Diversity Statement and Code Notebook v1.0, 2020; https://zenodo.org/record/3672110 (accessed on February 1, 2023).

# **□** Recommended by ACS

# **Engineering the Thermodynamic Stability and Metastability** of Mesophases of Colloidal Bipyramids through Shape **Entropy**

Yein Lim, Sharon C. Glotzer, et al.

FEBRUARY 28, 2023

ACS NANO

READ **C** 

# Bend-Induced Ferroelectric Domain Walls in α-In,Se<sub>3</sub>

Edmund Han, Pinshane Y. Huang, et al.

APRIL 14, 2023

ACS NANO

READ **C** 

#### Self-Assembling Systems for Optical Out-of-Plane Coupling **Devices**

Leonardo Z. Zornberg, Robert J. Macfarlane, et al.

FEBRUARY 08, 2023

ACS NANO

READ **C** 

# Mucus Penetration of Surface-Engineered Nanoparticles in Various pH Microenvironments

Yiyang Guo, Bingbing Sun, et al.

JANUARY 31, 2023

ACS NANO

READ 2

Get More Suggestions >